Low-Frequency Circulating Current Injection in Eight-Component Control for Modular Multilevel Matrix Converter Under Equal Frequency

Siyang Liu, *Graduate Student Member, IEEE*, Haotian Zhu, Xiangyu Zhao, Jiangpeng Yang, Jianglin Nie, and Zeliang Shu, *Senior Member, IEEE*

***Abstract*—The modular multilevel matrix converter ($\mathrm{M^3C}$) is a topology suitable for ac–ac fields, such as wind power conversion systems, large-capacity electric drives, etc. However, when the input frequency of the system is close to or equal to the output frequency, large voltage fluctuations even unbalancing will produce on the dc capacitors of the submodules, which limits the application range of $\mathrm{M^3C}$. This article proposes a low-frequency circulating current injection method to address the issue of dc capacitor voltage fluctuations in $\mathrm{M^3C}$ under equal frequency operating condition. The frequencies present within the $\mathrm{M^3C}$ are used to consist of the low-frequency circulation current. Therefore, the proposed method does not require injecting common mode voltage or applying reactive power. Experimental results based on the $\mathrm{M^3C}$ platform verify the effectiveness of the proposed method. Moreover, the dynamic performance is also good with the proposed control strategy under the conditions of output voltage or frequency change.**

***Index Terms*—Equal frequencies operation, internal circulation control, modular multilevel matrix converter ($\mathrm{M^3C}$).**

NOMENCLATURE

$U_{lx}/i_{lx}x = (a, b, c)$	Three-phase output voltages/currents.
$U_{sy}/i_{sy}y = (u, v, w)$	Three-phase input voltages/currents.
i_{xy}	Bridge arm current.
$U_{\mathrm{dc},xy}$	DC capacitor voltage.
P_{xy}	Bridge arm power.
$U_{\mathrm{OO'}}$	Common mode voltage.
$\mathrm{L_{arm}}$	Bridge arm inductor.
L_s	Input side inductor.
L_l	Output side inductor.
$\mathrm{C}_{\alpha\beta 0}$	Double $\alpha\beta 0$ transformation matrix.
$\mathrm{C_D}$	Diagonal transformation matrix.
U^*_{dc}	Reference value of the dc capacitor voltage.
φ	Phase shift between input and output voltage.
γ_s/γ_l	Phase shift between input/output voltage and current.

Manuscript received 26 April 2024; revised 2 July 2024; accepted 11 August 2024. Date of publication 20 August 2024; date of current version 7 October 2024. This work was supported in part by the National Key R&D Program of China under Grant 2021YFB2601500 and in part by the National Natural Science Foundation of China under Grant 52077183. Recommended for publication by Associate Editor A. Rao Dekka. *(Corresponding author: Zeliang Shu.)*

The authors are with the School of Electrical Engineering, Southwest Jiaotong University, Chengdu, Sichuan 610031, China (e-mail: siyangliu@my.swjtu.edu.cn; zht@my.swjtu.edu.cn; xiangyuzhao@my.swjtu.edu.cn; yjp_pe@my.swjtu.edu.cn; jacksonen@my.swjtu.edu.cn; shuzeliang@swjtu.edu.cn).

Color versions of one or more figures in this article are available at https://doi.org/10.1109/TPEL.2024.3444477.

Digital Object Identifier 10.1109/TPEL.2024.3444477

I. INTRODUCTION

MODULAR multilevel topologies have a great tendency in the application for smart grid, new energy, rail transportation, etc [1], [2], [3], [4], [5], [6]. Modular multilevel matrix converter ($\mathrm{M^3C}$) as one of the representative topologies, compared to traditional topologies, it has better performance, such as modularity, high power quality, and control flexibility [7], [8]. In ac to ac power conversion, $\mathrm{M^3C}$ has no common dc-link part such as dc-link capacitors and medium-frequency transformer (MFT), which can reduce the weight and size compared with back-to-back modular multilevel converter (MMC) and multistage power electronic transformer (PET) [9].

As a direct ac/ac converter, the voltage and current of input/output in $\mathrm{M^3C}$ are coupled. Therefore, the double α $\beta 0$ transformation [10], [11] is proposed to effectively solve the above problem. Hayashi et al. [12] and Nakamori et al. [13] proposed to equivalent the $\mathrm{M^3C}$ topology to three-phase cascaded H-bridge topologies for control. In [14], the double *dq* decoupling method is proposed for independent control of active and reactive power in $\mathrm{M^3C}$ also achieved. However, $\mathrm{M^3C}$ suffers a great problem with large dc capacitor voltage fluctuations even unbalancing when input and output frequencies are close or even equal. This may lead the system to crash in serious unbalance, thereby limiting the application of $\mathrm{M^3C}$ [15], [16], [17].

To address this issue, various methods have been proposed to stabilize the dc capacitor voltage under equal frequencies mode (EFM). Miura et al.[18], [19] adopted SVPWM modulation to avoid the circulating current path under EFM, thereby eliminating the fluctuation and unbalancing of dc capacitor voltage. However, the above SVPWM method avoids the problem of dc capacitor voltage unbalancing under EFM by cutting off the circulating current circuit. This undoubtedly reduces the utilization efficiency of submodules. In addition, as the number of submodules in the bridge arm increases, the complexity of the SVPWM method also increases. Kawamura et al. [20], [21] derived the voltage equalization condition of the system under EFM, and achieved stable and balance capacitor voltage by controlling the excitation current on the output side. However, this method needs to meet the conditions of equal input and output

voltage amplitudes and opposite initial phase angles. Therefore, a motor-magnetizing-current controller is adopted to achieve the above conditions. Subsequently, a method of injecting high-frequency circulating current into common mode voltage has been proposed [22], [23]. Although this method applies to most conditions, the use of common mode voltage injection may lead to premature motor bearing failures or the formation of leakage current in the motor casing, thereby affecting the insulation performance of the motor. Fan et al. [24] achieved the stable and balance of dc capacitor voltage under EFM by redistributing the bridge arm current, without injecting common mode voltage. What's more, a negative–negative sequence current component injection method was proposed in [25]. Subsequently, a method based on optimized predictive control was proposed to calculate the required circulating current and common mode voltage [26]. This method avoids the adverse effects of common mode voltage injection on the system. In [27], a continuous-control-set model predictive control for EFM is proposed. Furthermore, Cuzmar et al.[28] incorporates nominal current limits as bound constraints in the optimal control problem of MPC. However, this type of model prediction method has the disadvantage of heavy computational burden, which means it is not beneficial for digital implementation and industrial applications.

In this article, a low-frequency circulating current injection method in eight-component branch control based on double $\alpha\,\beta 0$ decoupling is proposed. This method can achieve dc capacitor voltage balance and stable operation of $\mathrm{M^3C}$ under EFM, which is the most severe condition of capacitor voltage fluctuations. This article divides the circulating power into eight components and derives its expression in detail under the double $\alpha\,\beta 0$ frame. Based on this, the low-frequency circulating current injection method for branch power control is proposed, which is different from the method mentioned above. Each branch is injected with different low-frequency circulating currents to compensate for the branch power unbalance that occurs under EFM. In addition, this method applies the frequency present in the system to consist of the low-frequency circulating current rather than injecting common mode voltage or applying reactive power.

The rest of this article is organized as follows. A basic introduction and double $\alpha\,\beta 0$ decoupling model to $\mathrm{M^3C}$ is illustrated in Section II. In Section III, the eight-component branch control method is illustrated. Simulation and experimental results under EFM are provided in Sections IV and V respectively. Finally, Section VI concludes this article.

II. System Description of the $\mathrm{M^3C}$

The circuit topology of $\mathrm{M^3C}$ is shown in Fig. 1. The system consists of nine bridge arms. Each bridge arm consists of N H-bridge submodules and one bridge arm inductor $\mathrm{L_{arm}}$. Each bridge arm is connected to the grid through a filter inductor $\mathrm{L}_i (i = s, l)$. U_{su}, U_{sv}, U_{sw} are the three-phase input voltages, i_{su}, i_{sv}, i_{sw} are the three-phase input currents;

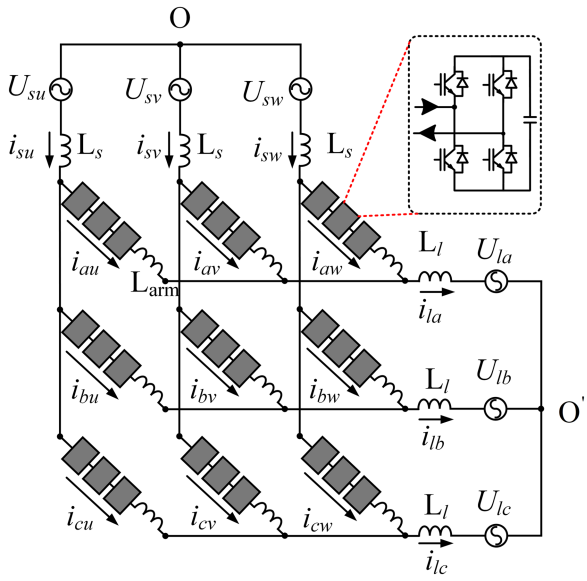

Fig. 1. Circuit topology of $\mathrm{M^3C}$.

U_{la}, U_{lb}, U_{lc} are the three-phase output voltages, i_{la}, i_{lb}, i_{lc} are the three-phase output currents; O, O′ are the neutral points of the three-phase system on the input and output sides, respectively; i_{xy} is the bridge arm current, where $x = (a, b, c)$, $y = (u, v, w)$.

A. Double $\alpha\beta 0$ Decoupling

As shown in Fig. 1, by applying Kirchhoff voltage laws (KVL) and double $\alpha\beta 0$ decoupling [15], [21], the mathematical model of $\mathrm{M^3C}$ can be obtained in (1), which is shown at the bottom of this page.

Where $i_{0\alpha}$ and $i_{0\beta}$ are only related to the input side while $i_{\alpha 0}$ and $i_{\beta 0}$ only related to the output side, which ensures the input and output side can be controlled independently. Besides, $i_{\alpha\alpha}$, $i_{\alpha\beta}$, $i_{\beta\alpha}$, and $i_{\beta\beta}$ are circulating currents which have no effect on the input or output side. Besides, in three-phase symmetrical system, $U_{s0} = i_{s0} = U_{l0} = i_{l0} = 0$. There is no current circuit between neutral points O and O′, so $i_{00} = 0$.

B. Steady-State Analysis of Bridge Arm DC Capacitor Voltage of $\mathrm{M^3C}$

Each module's dc capacitor voltage of $\mathrm{M^3C}$ under EFM are shown in Fig. 2. It can be noticed that the dc capacitor voltage

$$\sqrt{3}\begin{bmatrix} 0 & 0 & 0 \\ 0 & 0 & 0 \\ U_{s\alpha} & U_{s\beta} & U_{s0} \end{bmatrix} - \sqrt{3}\mathrm{L}_s \frac{d}{dt}\begin{bmatrix} 0 & 0 & 0 \\ 0 & 0 & 0 \\ i_{s\alpha} & i_{s\beta} & i_{s0} \end{bmatrix} = \mathrm{L_{arm}} \frac{d}{dt}\begin{bmatrix} i_{\alpha\alpha} & i_{\alpha\beta} & i_{\alpha 0} \\ i_{\beta\alpha} & i_{\beta\beta} & i_{\beta 0} \\ i_{0\alpha} & i_{0\beta} & i_{00} \end{bmatrix} + \begin{bmatrix} U_{\alpha\alpha} & U_{\alpha\beta} & U_{\alpha 0} \\ U_{\beta\alpha} & U_{\beta\beta} & U_{\beta 0} \\ U_{0\alpha} & U_{0\beta} & U_{00} \end{bmatrix}$$
$$+ \sqrt{3}\mathrm{L}_l \frac{d}{dt}\begin{bmatrix} 0 & 0 & i_{l\alpha} \\ 0 & 0 & i_{l\beta} \\ 0 & 0 & i_{l0} \end{bmatrix} + \sqrt{3}\begin{bmatrix} 0 & 0 & U_{l\alpha} \\ 0 & 0 & U_{l\beta} \\ 0 & 0 & U_{l0} \end{bmatrix} + U_{\mathrm{OO'}}\begin{bmatrix} 0 & 0 & 0 \\ 0 & 0 & 0 \\ 0 & 0 & 3 \end{bmatrix}. \quad (1)$$

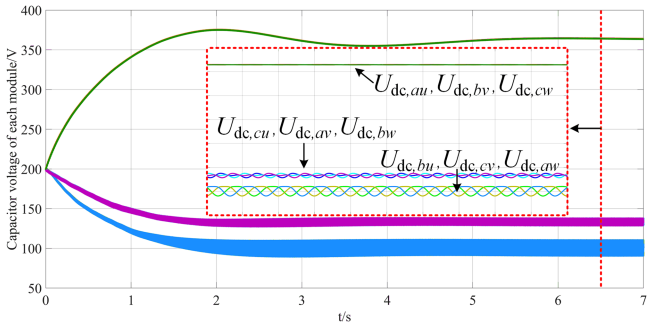

Fig. 2. Capacitor voltage of each module under EFM.

of the bridge arm module deviates from the reference value of 200 V under EFM. Therefore, it is necessary to analyze the bridge arm dc capacitor voltage.

The submodule of M^{3}C is a full bridge H-bridge module. Assuming that the dc capacitance value and capacitance voltage are both the same, then the total voltage change of each capacitor in the bridge arm $\Delta U_{\mathrm{dc},xy}$ can be expressed as follows:

$$\Delta U_{\mathrm{dc},xy} = \sum \Delta U_{\mathrm{dc}} = \int \frac{N \cdot P_{xy}}{C \cdot U_{\mathrm{dc},xy}} dt \tag{2}$$

where P_{xy} represents the power flowing through the bridge arm, $U_{\mathrm{dc},xy}$ represents the total capacitance–voltage of the bridge arm.

Assuming that the input voltage and current are three-phase symmetrical during stable system operation, the input voltage and input current can be expressed as follows:

$$\begin{cases} U_{sy} = U_s \sin(\omega_s t + \delta_y) \\ i_{sy} = I_s \sin(\omega_s t - \gamma_s + \delta_y) \end{cases} \tag{3}$$

where $y = (u, v, w)$, δ_y is the phase shift of three-phase input voltage, $\delta_u = 0$, $\delta_v = -2\pi/3$, $\delta_w = 2\pi/3$. γ_s is the phase shift between input voltage and current.

Similarly, the output voltage and output current can be expressed as follows:

$$\begin{cases} U_{lx} = U_l \sin(\omega_l t + \delta_x - \varphi) \\ i_{lx} = I_l \sin(\omega_l t - \gamma_l + \delta_x - \varphi) \end{cases} \tag{4}$$

where $x = (a, b, c)$, δ_x is the phase shift of three-phase output voltage, $\delta_a = 0$, $\delta_b = -2\pi/3$, $\delta_c = 2\pi/3$, γ_l is the phase shift between output voltage and current. φ is the phase shift between input voltage and output voltage.

From Fig. 1, the expression between the bridge arm current bridge i_{xy} and the input/output current can be obtained

$$\begin{cases} i_{su} = i_{au} + i_{bu} + i_{cu} \\ i_{sv} = i_{av} + i_{bv} + i_{vc} \\ i_{sw} = i_{wa} + i_{bw} + i_{cw} \\ i_{la} = i_{au} + i_{av} + i_{aw} \\ i_{lb} = i_{bu} + i_{bv} + i_{bw} \\ i_{lc} = i_{cu} + i_{cv} + i_{cw} \end{cases}. \tag{5}$$

Assuming that there is no circulating current component between the bridge arms in the M^{3}C system, and the three-phase input voltage, input current, and three-phase output voltage and output current are completely symmetrical, it can be obtained

$$i_{xy} = \frac{1}{3} i_{sy} + \frac{1}{3} i_{lx}. \tag{6}$$

Assuming that there is no circulation component between bridge arms in M^{3}C, the instantaneous power P_{xy} of the xy bridge arm in the system can be expressed as follows:

$$P_{xy} = (U_{sy} - U_{lx}) \cdot \frac{1}{3}(i_{sy} + i_{lx}). \tag{7}$$

Taking the au bridge arm as an example, combining (2), (3), (4), and (7), the change in capacitor voltage $\Delta U_{\mathrm{dc},au}$ of the bridge arm au can be obtained as follows.

1) The input/output double-frequency component: The input frequency twice component $\Delta U_{2fs,au}$, and the output frequency twice component $\Delta U_{2fl,au}$ can be expressed as follows:

$$\begin{cases} \Delta U_{2fs,au} = \dfrac{-NU_s I_s \sin(2\omega_s t - \gamma_s)}{6 \cdot 2\omega_s C U_{\mathrm{dc},au}} \\ \Delta U_{2fl,au} = \dfrac{NU_l I_l \sin(2\omega_l t - \gamma_l + 2\varphi)}{6 \cdot 2\omega_l C U_{\mathrm{dc},au}} \end{cases}. \tag{8}$$

2) The sum/difference between input and output frequencies component: The difference between input and output frequencies component $\Delta U_{fs-fl,au}$, and the sum between input and output frequencies component $\Delta U_{fs+fl,au}$ can be expressed as follows:

$$\begin{cases} \Delta U_{fs-fl,au} = \dfrac{NU_s I_l \sin[(\omega_s - \omega_l)t + \gamma_l - \varphi]}{6 \cdot (\omega_s - \omega_l) C U_{\mathrm{dc},au}} \\ \qquad\qquad - \dfrac{NU_l I_s \sin[(\omega_s - \omega_l)t - \gamma_s - \varphi]}{6 \cdot (\omega_s - \omega_l) C U_{\mathrm{dc},au}} \\ \Delta U_{fs+fl,au} = \dfrac{-NU_s I_l \sin[(\omega_s + \omega_l)t - \gamma_l + \varphi]}{6 \cdot (\omega_s + \omega_l) C U_{\mathrm{dc},au}} \\ \qquad\qquad + \dfrac{NU_l I_s \sin[(\omega_s + \omega_l)t - \gamma_s + \varphi]}{6 \cdot (\omega_s + \omega_l) C U_{\mathrm{dc},au}} \end{cases}. \tag{9}$$

Consider setting input frequency $f_s = 50\,\mathrm{Hz}$, the number of submodules $N = 1$, module capacitance $C = 1\,\mathrm{mF}$, peak input voltage $U_s = 100\,\mathrm{V}$, peak input current $I_s = 3.6\,\mathrm{A}$, peak output voltage $U_l = 60\,\mathrm{V}$, peak output current $I_l = 6\,\mathrm{A}$, capacitance voltage amplitude $U_{\mathrm{dc},au} = 200\,\mathrm{V}$, and phase angle $\gamma_s = \gamma_l = \varphi = 0$. The relationship between the amplitude of each frequency component of the capacitor voltage $|\Delta U_{2fs,au}|$, $|\Delta U_{2fl,au}|$, $|\Delta U_{fs-fl,au}|$, and $|\Delta U_{fs+fl,au}|$ with the output frequency f_l is shown in Fig. 2.

From Fig. 3, it can be noticed that the frequency component of the capacitor voltage in the M^{3}C system is unstable under special operating conditions of $f_l = 0\,\mathrm{Hz}$ or $f_s = f_l$, which leading to power unbalance in the system. Therefore, it is necessary to decouple the power of M^{3}C and add additional control to achieve power balance of the system at special operating points $f_s = f_l$.

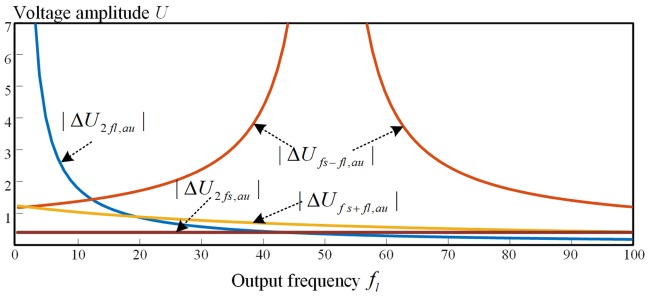

Fig. 3. Relationship between the amplitude of each frequency component and the output frequency.

C. Power Decoupling of M³C

After double $\alpha\ \beta 0$ decoupling, the bridge arm power can be expressed as

$$\begin{bmatrix} P_{\alpha\alpha} & P_{\alpha\beta} & P_{\alpha 0} \\ P_{\beta\alpha} & P_{\beta\beta} & P_{\beta 0} \\ P_{0\alpha} & P_{0\beta} & P_{00} \end{bmatrix} = \mathrm{C}_{\alpha\beta 0} \cdot \begin{bmatrix} U_{au}i_{au} & U_{av}i_{av} & U_{aw}i_{aw} \\ U_{bu}i_{bu} & U_{bv}i_{bv} & U_{bw}i_{bw} \\ U_{cu}i_{cu} & U_{cv}i_{cv} & U_{cw}i_{cw} \end{bmatrix} \cdot \mathrm{C}_{\alpha\beta 0}^{\mathrm{T}}. \tag{10}$$

Considering the relationship between the bridge arm current and the input/output currents of the node, combined with the calculation process of double $\alpha\ \beta 0$ decoupling, it can be obtained that

$$i_{\alpha 0} = \frac{i_{l\alpha}}{\sqrt{3}}, i_{\beta 0} = \frac{i_{l\beta}}{\sqrt{3}}, i_{0\alpha} = \frac{i_{s\alpha}}{\sqrt{3}}, i_{0\beta} = \frac{i_{s\beta}}{\sqrt{3}}. \tag{11}$$

Therefore, combining (1) and (11), it can be obtained that

$$\begin{bmatrix} U_{au} & U_{av} & U_{aw} \\ U_{bu} & U_{bv} & U_{bw} \\ U_{cu} & U_{cv} & U_{cw} \end{bmatrix} = \mathrm{C}_{\alpha\beta 0}^{\mathrm{T}} \cdot \begin{bmatrix} 0 & 0 & -\sqrt{3}U_{l\alpha} \\ 0 & 0 & -\sqrt{3}U_{l\beta} \\ \sqrt{3}U_{s\alpha} & \sqrt{3}U_{s\beta} & -3U_{\mathrm{OO}'} \end{bmatrix} \cdot \mathrm{C}_{\alpha\beta 0} \tag{12}$$

$$\begin{bmatrix} i_{au} & i_{av} & i_{aw} \\ i_{bu} & i_{bv} & i_{bw} \\ i_{cu} & i_{cv} & i_{cwb} \end{bmatrix} = \mathrm{C}_{\alpha\beta 0}^{\mathrm{T}} \cdot \begin{bmatrix} i_{\alpha\alpha} & i_{\alpha\beta} & i_{l\alpha}/\sqrt{3} \\ i_{\beta\alpha} & i_{\beta\beta} & i_{l\beta}/\sqrt{3} \\ i_{s\alpha}/\sqrt{3} & i_{s\beta}/\sqrt{3} & i_{00} \end{bmatrix} \cdot \mathrm{C}_{\alpha\beta 0} \tag{13}$$

where there is no current circuit between neutral points O and O′, $i_{00} = 0$. What's more, because this article does not use common mode voltage injection method, it is believed that $U_{\mathrm{OO}'} = 0$.

Combining (10), (12), and (13), the bridge arm power for double $\alpha\ \beta 0$ decoupling can be easily obtained as shown follows:

$$P_{\alpha\alpha} = \frac{(U_{s\alpha}i_{l\alpha} - U_{l\alpha}i_{s\alpha})}{3} + \frac{(U_{s\alpha}i_{\alpha\alpha} - U_{s\beta}i_{\alpha\beta})}{\sqrt{6}} - \frac{(U_{l\alpha}i_{\alpha\alpha} - U_{l\beta}i_{\alpha\beta})}{\sqrt{6}} \tag{14}$$

$$P_{\alpha\beta} = \frac{(U_{s\beta}i_{l\alpha} - U_{l\alpha}i_{s\beta})}{3} - \frac{(U_{s\alpha}i_{\alpha\beta} + U_{s\beta}i_{\alpha\alpha})}{\sqrt{6}} - \frac{(U_{l\alpha}i_{\alpha\beta} - U_{l\beta}i_{\beta\beta})}{\sqrt{6}} \tag{15}$$

$$P_{\beta\alpha} = \frac{(U_{s\alpha}i_{l\beta} - U_{l\beta}i_{s\alpha})}{3} + \frac{(U_{s\alpha}i_{\beta\alpha} - U_{s\beta}i_{\beta\beta})}{\sqrt{6}} + \frac{(U_{l\alpha}i_{\beta\alpha} + U_{l\beta}i_{\alpha\alpha})}{\sqrt{6}} \tag{16}$$

$$P_{\beta\beta} = \frac{(U_{s\beta}i_{l\beta} - U_{l\beta}i_{s\beta})}{3} - \frac{(U_{s\alpha}i_{\beta\beta} + U_{s\beta}i_{\beta\alpha})}{\sqrt{6}} + \frac{(U_{l\alpha}i_{\beta\beta} + U_{l\beta}i_{\alpha\beta})}{\sqrt{6}} \tag{17}$$

$$P_{\alpha 0} = \frac{(U_{s\alpha}i_{\alpha\alpha} + U_{s\beta}i_{\alpha\beta})}{\sqrt{3}} - \frac{\sqrt{2}\,(U_{l\alpha}i_{l\alpha} - U_{l\beta}i_{l\beta})}{6} \tag{18}$$

$$P_{\beta 0} = \frac{(U_{s\alpha}i_{\beta\alpha} + U_{s\beta}i_{\beta\beta})}{\sqrt{3}} + \frac{\sqrt{2}\,(U_{l\alpha}i_{l\beta} + U_{l\beta}i_{l\alpha})}{6} \tag{19}$$

$$P_{0\alpha} = -\frac{(U_{l\alpha}i_{\alpha\alpha} + U_{l\beta}i_{\alpha\beta})}{\sqrt{3}} + \frac{\sqrt{2}\,(U_{s\alpha}i_{s\alpha} - U_{s\beta}i_{s\beta})}{6} \tag{20}$$

$$P_{0\beta} = -\frac{(U_{l\alpha}i_{\alpha\beta} + U_{l\beta}i_{\beta\beta})}{\sqrt{3}} - \frac{\sqrt{2}\,(U_{s\alpha}i_{s\beta} + U_{s\beta}i_{s\alpha})}{6} \tag{21}$$

$$P_{00} = \frac{(U_{s\alpha}i_{s\alpha} + U_{s\beta}i_{s\beta})}{3} - \frac{(U_{l\alpha}i_{l\alpha} + U_{l\beta}i_{l\beta})}{3}. \tag{22}$$

However, the four circulating currents of $i_{\alpha\alpha}, i_{\alpha\beta}, i_{\beta\alpha}, i_{\beta\beta}$ still couple two frequency components, $\omega_{s-l}, \omega_{s+l}$ [15]. Therefore, additional transformations are needed to reduce coupling. This transformation method is called diagonal transformation [15]. The decoupling method of circulation is as follows:

$$\begin{bmatrix} i_{d1\alpha} \\ i_{d1\beta} \\ i_{d2\alpha} \\ i_{d2\beta} \end{bmatrix} = \mathrm{C_D} \cdot \begin{bmatrix} i_{\alpha\alpha} \\ i_{\alpha\beta} \\ i_{\beta\alpha} \\ i_{\beta\beta} \end{bmatrix}, \mathrm{C_D} = \frac{1}{2}\begin{bmatrix} 1 & 0 & 0 & 1 \\ 0 & 1 & -1 & 0 \\ 1 & 0 & 0 & -1 \\ 0 & 1 & 1 & 0 \end{bmatrix}. \tag{23}$$

Using diagonal transformations in (14)–(17), the decoupled bridge arm power can be expressed as shown follows:

$$P_{d1\alpha} = \frac{U_{s\alpha}i_{l\alpha} - U_{l\alpha}i_{s\alpha}}{6} + \frac{U_{s\beta}i_{l\beta} - U_{l\beta}i_{s\beta}}{6} + \frac{U_{s\alpha}i_{d2\alpha} - U_{s\beta}i_{d2\beta}}{\sqrt{6}} - \frac{U_{l\alpha}i_{d2\alpha} - U_{l\beta}i_{d2\beta}}{\sqrt{6}} \tag{24}$$

$$P_{d1\beta} = -\frac{U_{s\alpha}i_{l\beta} + U_{l\alpha}i_{s\beta}}{6} + \frac{U_{s\beta}i_{l\alpha} + U_{l\beta}i_{s\alpha}}{6} - \frac{U_{s\alpha}i_{d2\beta} + U_{s\beta}i_{d2\alpha}}{\sqrt{6}} - \frac{U_{l\alpha}i_{d2\beta} + U_{l\beta}i_{d2\alpha}}{\sqrt{6}} \tag{25}$$

$$P_{d2\alpha} = \frac{U_{s\alpha}i_{l\alpha} - U_{l\alpha}i_{s\alpha}}{6} - \frac{U_{s\beta}i_{l\beta} - U_{l\beta}i_{s\beta}}{6} + \frac{U_{s\alpha}i_{d1\alpha} - U_{s\beta}i_{d1\beta}}{\sqrt{6}} - \frac{U_{l\alpha}i_{d1\alpha} - U_{l\beta}i_{d1\beta}}{\sqrt{6}} \tag{26}$$

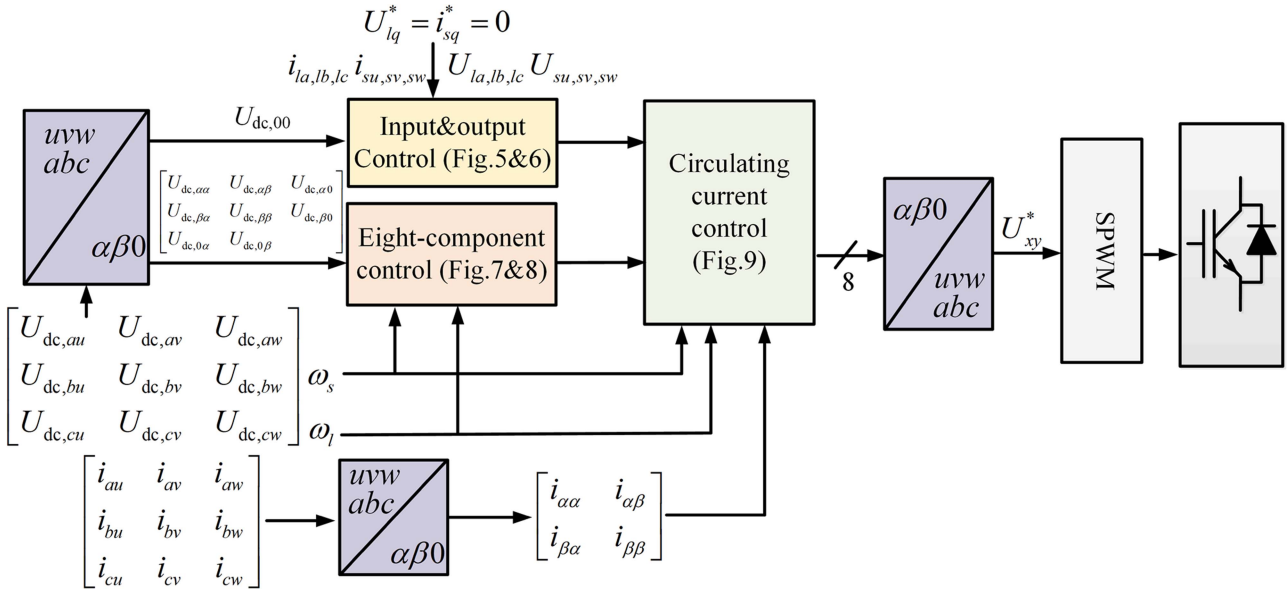

Fig. 4. Overall control block diagram of M^{3}C.

$$P_{d2\beta}=\frac{U_{s\alpha}i_{l\beta}-U_{l\alpha}i_{s\beta}}{6}+\frac{U_{s\beta}i_{l\alpha}-U_{l\beta}i_{s\alpha}}{6}-\frac{U_{s\alpha}i_{d1\beta}+U_{s\beta}i_{d1\alpha}}{\sqrt{6}}-\frac{U_{l\alpha}i_{d1\beta}+U_{l\beta}i_{d1\alpha}}{\sqrt{6}} \tag{27}$$

$$P_{\alpha 0}=\frac{U_{s\alpha}\left(i_{d1\alpha}+i_{d2\alpha}\right)}{\sqrt{3}}+\frac{U_{s\beta}\left(i_{d1\beta}+i_{d2\beta}\right)}{\sqrt{3}}-\frac{\sqrt{2}\left(U_{l\alpha}i_{l\alpha}-U_{l\beta}i_{l\beta}\right)}{6} \tag{28}$$

$$P_{\beta 0}=\frac{U_{s\alpha}\left(i_{d1\alpha}+i_{d2\alpha}\right)}{\sqrt{3}}+\frac{U_{s\beta}\left(i_{d1\beta}+i_{d2\beta}\right)}{\sqrt{3}}+\frac{\sqrt{2}\left(U_{l\alpha}i_{l\beta}+U_{l\beta}i_{l\alpha}\right)}{6} \tag{29}$$

$$P_{0\alpha}=-\frac{U_{l\alpha}\left(i_{d1\alpha}+i_{d2\alpha}\right)}{\sqrt{3}}-\frac{U_{l\beta}\left(-i_{d1\beta}+i_{d2\beta}\right)}{\sqrt{3}}+\frac{\sqrt{2}\left(U_{s\alpha}i_{s\alpha}-U_{s\beta}i_{s\beta}\right)}{6} \tag{30}$$

$$P_{0\beta}=-\frac{U_{l\alpha}\left(i_{d1\beta}+i_{d2\beta}\right)}{\sqrt{3}}-\frac{U_{l\beta}\left(i_{d1\alpha}-i_{d2\alpha}\right)}{\sqrt{3}}-\frac{\sqrt{2}\left(U_{s\alpha}i_{s\beta}+U_{s\beta}i_{s\alpha}\right)}{6}. \tag{31}$$

From (24)–(31), it can be noticed that, the components of bridge arm power can be divided into two categories.

1) Uncontrollable parts are composed of input and output components, such as $U_{s\alpha}$, $i_{s\alpha}$, $U_{s\beta}$, $i_{s\beta}$. These components cannot adjust power without affecting the input or output ports.
2) Controllable parts such as the four circulations currents of $i_{d1\alpha}, i_{d1\beta}, i_{d2\alpha}, i_{d2\beta}$. These circulating currents can work together with the input and output voltages to adjust the power of the M^{3}C bridge arm without affecting the input and output ports.

Therefore, it is possible to eliminate the power unbalance of the bridge arm in the system under EFM by controlling the circulating currents.

III. Low-Frequency Circulating Current Injection Method of the M^{3}C

The proposed overall control block diagram is shown in Fig. 4. Each controller is described in the following sections.

A. Input/Output Control of M^{3}C

Assuming that the capacitance-voltage of nine bridge arms is stable at the reference value $U_{\rm dc}^{*}$, it can be obtained that

$$\begin{bmatrix} U_{\rm dc,\alpha\alpha}^{*} & U_{\rm dc,\alpha\beta}^{*} & U_{\rm dc,\alpha 0}^{*} \\ U_{\rm dc,\beta\alpha}^{*} & U_{\rm dc,\beta\beta}^{*} & U_{\rm dc,\beta 0}^{*} \\ U_{\rm dc,0\alpha}^{*} & U_{\rm dc,0\beta}^{*} & U_{\rm dc,00}^{*} \end{bmatrix}=\begin{bmatrix} 0 & 0 & 0 \\ 0 & 0 & 0 \\ 0 & 0 & 3NU_{\rm dc}^{*} \end{bmatrix}. \tag{32}$$

According to (32), it can be noticed that under double α $\beta 0$ frame, $U_{\rm dc,00}^{*}$ represents the total voltage of nine bridge arm capacitors and can be used for total capacitor voltage control. Therefore, the input/output control of M^{3}C is shown in Figs. 5 and 6.

Where $U_{\rm dc}^{*}$ is the reference value for the capacitor voltage of each module. U_{ld}^{*} is the reference value for the amplitude of the output side voltage. The d-axis reference current is calculated by the PI controller to control the total capacitance–voltage of the submodule. The q-axis current reference is set to 0 to ensure unit power factor operation.

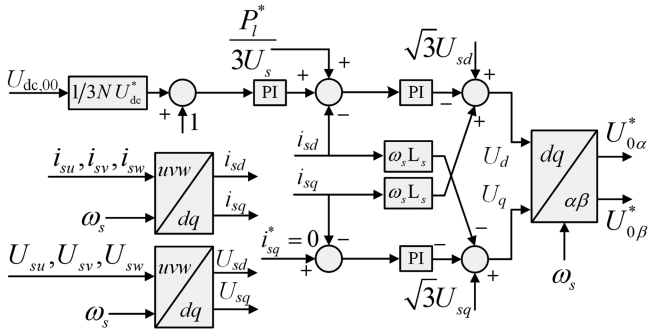

Fig. 5. Input control block diagram of M^{3}C.

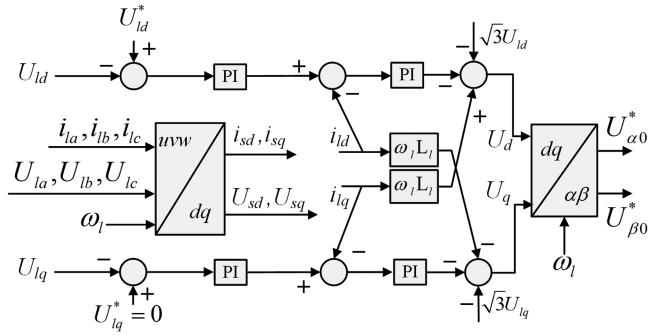

Fig. 6. Output control block diagram of M^{3}C.

B. Balanced Voltage Control Between Bridge Arms of M^{3}C

According to (32), it can be noticed that $U_{\mathrm{dc},\alpha\alpha}$, $U_{\mathrm{dc},\alpha\beta}$, $U_{\mathrm{dc},\alpha 0}$, $U_{\mathrm{dc},\beta\alpha}$, $U_{\mathrm{dc},\beta\beta}$, $U_{\mathrm{dc},\beta 0}$, $U_{\mathrm{dc},0\alpha}$, $U_{\mathrm{dc},0\beta}$ reflect the degree of unbalance between the voltage of the nine bridge arm capacitors and need to be controlled to 0. Therefore, the eight-component branch control method is proposed to achieve bridge arm power balance.

According to the double α $\beta 0$ transformation, it can be obtained that

$$\begin{cases} U_{i\alpha} = \sqrt{\dfrac{3}{2}} V_i \cdot \mathrm{Sin}\left(\theta_i\right) \\ U_{i\beta} = -\sqrt{\dfrac{3}{2}} V_i \cdot \mathrm{Cos}\left(\theta_i\right) \\ i_{j\alpha} = \sqrt{\dfrac{3}{2}} I_j \cdot \mathrm{Sin}\left(\theta_j\right) \\ i_{j\beta} = -\sqrt{\dfrac{3}{2}} I_j \cdot \mathrm{Cos}\left(\theta_j\right) \end{cases} \tag{33}$$

where $\theta = \omega t$, $i = (s, l)$, $j = (s, l, d1, d2)$. Substitute (33) into (24)–(31), the decoupled bridge arm power can be divided into the following two parts:

The sum/difference of input and output frequencies component can be described as

$$P_{d1\alpha} = \frac{1}{4}\left[V_s I_l \cos\left(\theta_s - \theta_l\right) - V_l I_s \cos\left(\theta_s - \theta_l\right)\right] + \frac{\sqrt{6}}{4}\left[-V_s I_{d2} \cos\left(\theta_s + \theta_{d2}\right) + V_l I_{d2} \cos\left(\theta_l + \theta_{d2}\right)\right] \tag{34}$$

$$P_{d1\beta} = \frac{1}{4}\left[V_s I_l \sin\left(\theta_s - \theta_l\right) - V_l I_s \sin\left(\theta_s - \theta_l\right)\right] + \frac{\sqrt{6}}{4}\left[V_s I_{d2} \sin\left(\theta_s + \theta_{d2}\right) + V_l I_{d2} \sin\left(\theta_m + \theta_{d2}\right)\right] \tag{35}$$

$$P_{d2\alpha} = \frac{1}{4}\left[-V_s I_l \cos\left(\theta_s + \theta_l\right) + V_l I_s \cos\left(\theta_s + \theta_l\right)\right] + \frac{\sqrt{6}}{4}\left[-V_s I_{d1} \cos\left(\theta_s + \theta_{d1}\right) - V_l I_{d1} \cos\left(\theta_l - \theta_{d1}\right)\right] \tag{36}$$

$$P_{d2\beta} = \frac{1}{4}\left[-V_s I_l \sin\left(\theta_s + \theta_l\right) + V_l I_s \sin\left(\theta_s + \theta_l\right)\right] + \frac{\sqrt{6}}{4}\left[V_s I_{d1} \sin\left(\theta_s + \theta_{d1}\right) + V_l I_{d1} \sin\left(\theta_l - \theta_{d1}\right)\right]. \tag{37}$$

It can be observed that $P_{d1\alpha}$, and $P_{d1\beta}$ only contain differential frequency components, i.e., $\theta_s - \theta_l$. $P_{d2\alpha}$, and $P_{d2\beta}$ only contain sum frequency components, i.e., $\theta_s + \theta_l$. $P_{\alpha 0}$, and $P_{\beta 0}$ only contain two times the frequency of output-side components, i.e., $2\theta_l$. $P_{0\alpha}$, and $P_{0\beta}$ only contain two times the frequency of input-side components, i.e., $2\theta_s$. What's more, it can be noticed that (34)–(37) can be further decoupled in the dq frame

$$P_{d1d} = -\frac{\sqrt{6}}{4}\left[V_s I_{d2} \sin\left(2\theta_s - \theta_l + \theta_{d2}\right)\right] - \frac{\sqrt{6}}{4}\left[V_l I_{d2} \sin\left(2\theta_l - \theta_s + \theta_{d2}\right)\right] \tag{38}$$

$$P_{d1q} = \frac{1}{4}\left[V_s I_l - V_l I_s\right] - \frac{\sqrt{6}}{4}\left[V_s I_{d2} \cos\left(2\theta_s - \theta_l + \theta_{d2}\right)\right] + \frac{\sqrt{6}}{4}\left[V_l I_{d2} \cos\left(2\theta_l - \theta_s + \theta_{d2}\right)\right] \tag{39}$$

$$P_{d2d} = -\frac{\sqrt{6}}{4}\left[V_s I_{d1} \sin\left(2\theta_s + \theta_l + \theta_{d1}\right)\right] - \frac{\sqrt{6}}{4}\left[V_l I_{d1} \sin\left(2\theta_l + \theta_s - \theta_{d1}\right)\right] \tag{40}$$

$$P_{d2q} = \frac{1}{4}\left[-V_s I_l + V_l I_s\right] - \frac{\sqrt{6}}{4}\left[V_s I_{d1} \cos\left(2\theta_s + \theta_l + \theta_{d1}\right)\right] - \frac{\sqrt{6}}{4}\left[V_l I_{d1} \cos\left(2\theta_l + \theta_s - \theta_{d1}\right)\right]. \tag{41}$$

From (38) and (39), it can be observed that the dc component of the EFM power is concentrated in the reactive components P_{d1q}. Therefore, it is possible to set the frequency of i_{d2} to $\theta_{d2} = -2\theta_s + \theta_l$ recorded as i_{d2_1}, in order to offset the dc

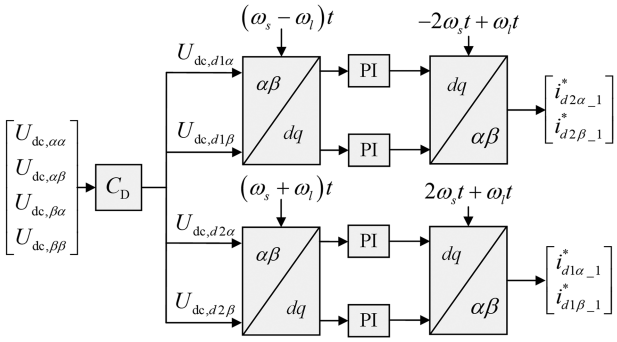

Fig. 7. Control block diagram of $U_{\mathrm{dc},d1\alpha}$, $U_{\mathrm{dc},d1\beta}$, $U_{\mathrm{dc},d1\alpha}$, and $U_{\mathrm{dc},d1\beta}$.

components in P_{d1d}, and P_{d1q} in M^{3}C. Similarly, according to (40) and (41), it is possible to set the frequency of i_{d1} in P_{d2d}, and P_{d2q} to $\theta_{d1}=2\theta_s+\theta_l$, recorded as i_{d1_1}. Moreover, due to $U_{\mathrm{dc}}=\frac{N}{CU^*_{\mathrm{dc}}}\int Pdt$, the reference value for the bridge arm power under double $\alpha\ \beta 0$ frame can be obtained as

$$\begin{bmatrix}\overline{P}^*_{\alpha\alpha} & \overline{P}^*_{\alpha\beta} & \overline{P}^*_{\alpha 0}\\ \overline{P}^*_{\beta\alpha} & \overline{P}^*_{\beta\beta} & \overline{P}^*_{\beta 0}\\ \overline{P}^*_{0\alpha} & \overline{P}^*_{0\beta} & \end{bmatrix} = \left(K_p+\frac{K_i}{s}\right)\cdot\left(-\begin{bmatrix}\overline{U}_{\mathrm{dc},\alpha\alpha} & \overline{U}_{\mathrm{dc},\alpha\beta} & \overline{U}_{\mathrm{dc},\alpha 0}\\ \overline{U}_{\mathrm{dc},\beta\alpha} & \overline{U}_{\mathrm{dc},\beta\beta} & \overline{U}_{\mathrm{dc},\beta 0}\\ \overline{U}_{\mathrm{dc},0\alpha} & \overline{U}_{\mathrm{dc},0\beta} & \end{bmatrix}\right). \tag{42}$$

Therefore, the control of the differential and sum of input and output frequencies component is shown in Fig. 7.

The input/output double-frequency component can be described as follows:

$$P_{\alpha 0}=\frac{\sqrt{2}}{4}V_l I_l\cos 2\theta_l+\frac{\sqrt{3}}{2}\left[V_s I_{d1}\cos\left(\theta_s-\theta_{d1}\right)\right]+\frac{\sqrt{3}}{2}\left[V_s I_{d2}\cos\left(\theta_s-\theta_{d2}\right)\right] \tag{43}$$

$$P_{\beta 0}=-\frac{\sqrt{2}}{4}V_l I_l\sin 2\theta_l-\frac{\sqrt{3}}{2}\left[V_s I_{d1}\sin\left(\theta_s-\theta_{d1}\right)\right]-\frac{\sqrt{3}}{2}\left[V_s I_{d2}\sin\left(\theta_s-\theta_{d2}\right)\right] \tag{44}$$

$$P_{0\alpha}=-\frac{\sqrt{2}}{4}V_s I_s\cos 2\theta_s+\frac{\sqrt{3}}{2}\left[V_l I_{d1}\cos\left(\theta_l+\theta_{d1}\right)\right]-\frac{\sqrt{3}}{2}\left[V_l I_{d2}\cos\left(\theta_l-\theta_{d2}\right)\right] \tag{45}$$

$$P_{0\beta}=\frac{\sqrt{2}}{4}V_s I_s\sin 2\theta_s+\frac{\sqrt{3}}{2}\left[V_l I_{d1}\sin\left(\theta_l+\theta_{d1}\right)\right]-\frac{\sqrt{3}}{2}\left[V_l I_{d2}\sin\left(\theta_l-\theta_{d2}\right)\right]. \tag{46}$$

From (43)–(46), it can be observed that it is possible to set the frequency of i_{d1} in $P_{\alpha 0}$, and $P_{\beta 0}$ to $\theta_{d1}=\theta_s$, recorded as i_{d1_2}; set the frequency of i_{d2} in $P_{0\alpha}$, and $P_{0\beta}$ to $\theta_{d2}=\theta_l$, recorded as i_{d2_2}. Therefore, it can achieve offset of the dc component in each component, respectively. The control of the input/output double frequency is shown in Fig. 8.

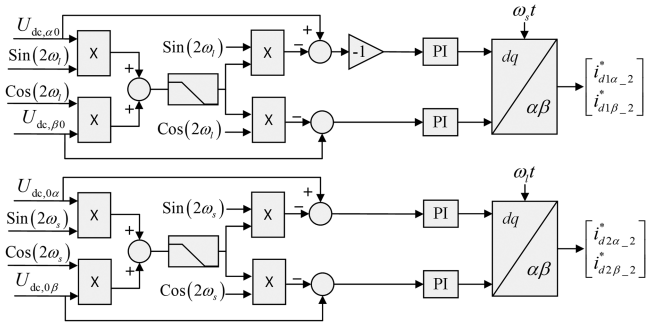

Fig. 8. Control block diagram of $U_{\mathrm{dc},\alpha 0}$, $U_{\mathrm{dc},\beta 0}$, $U_{\mathrm{dc},0\alpha}$, and $U_{\mathrm{dc},0\beta}$.

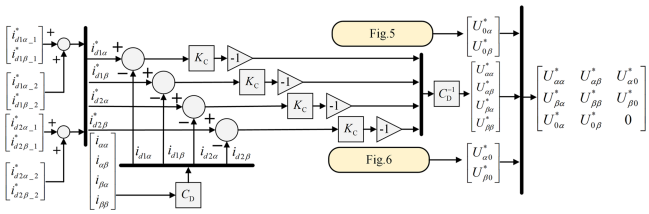

Fig. 9. Control block diagram of circulating current.

TABLE I
CIRCUIT PARAMETERS OF THE SYSTEM

Parameters	Symbol	Value
Input phase voltage (peak value)	U_s	100 V
Output phase voltage (peak value)	U_l	60 V
DC capacitor voltage	U_{dc}	200 V
Input frequency	f_s	50 Hz
Output frequency (DFM)	f_l	50/3 Hz
Output frequency (EFM)	f_l	50 Hz
Input/Output filter inductance	$\mathrm{L}_{u,v,w,a,b,c}$	5 mH
Bridge arm inductance	$\mathrm{L}_{\mathrm{arm}}$	1 mH
H-bridge DC capacitance	C	1 mF
Switching frequency	f	10 kHz
Three phase load	$\mathrm{R}_{a,b,c}$	10 Ω
Number of bridge arm modules	N	1

Combining Figs. 5 and 6, the control block diagram of circulating current is shown in Fig. 9. Where K_C is the proportional controller (P) parameter.

IV. SIMULATION RESULTS

To verify the proposed eight-component branch control method, the simulations of different input and output frequency mode (DFM) are first conducted in a MATLAB/Simulink environment. The simulation parameters of the adopted M^3 C system are shown in Table I.

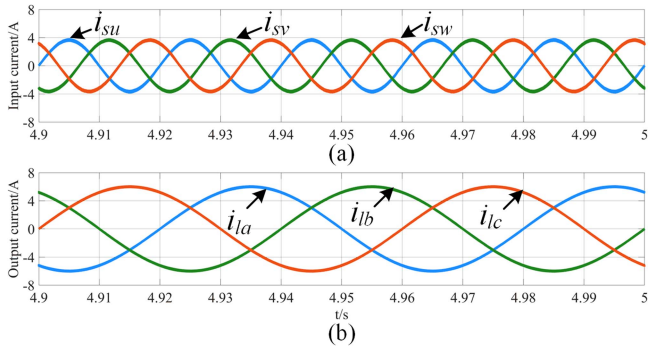

Fig. 10. Three-phase current under DFM.

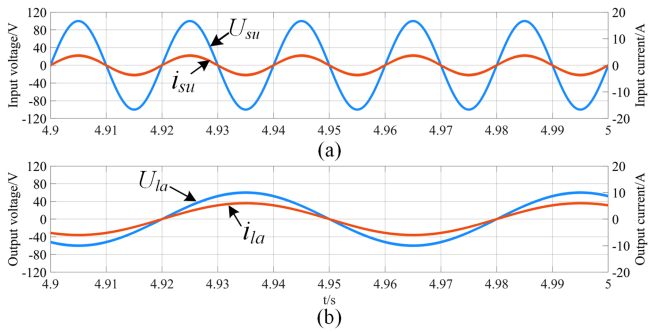

Fig. 11. Input and output voltage and current under DFM.

A. Different Frequencies Mode (DFM)

In the simulation model, the input frequency f_s is set to the grid voltage frequency 50 Hz, and the output frequency f_l is set to the commonly used transmission frequency in the low frequency alternating current (LFAC) system, which is 50/3 Hz. The three-phase currents are shown in Fig. 10.

Where the input currents are shown in Fig. 10(a), and the THD of i_{su}, i_{sv}, and i_{sw} are 1.96%, 2.02%, and 1.97%, respectively. The output currents are shown in Fig. 10(b), and the THD of i_{la}, i_{lb}, and i_{lc} are 0.56%, 0.55%, and 0.57%, respectively. It can be noticed that in the simulation, the input and output currents of the M^3C almost do not contain other harmonic components, which means that the control method proposed in this article does not affect the power quality of the system. The voltage and current are shown in Fig. 11. It can be noticed from Fig. 11(a) that the phase of the input voltage U_{su} and current i_{su} is the same, which means the system operates under the unit power factor. The output voltage and current are shown in Fig. 11(b), with the resistive system output.

The dc capacitor voltages of each module are shown in Fig. 12. It can be noticed that the voltage of the module capacitor is stable at the reference value of 200 V, and the maximum voltage fluctuation of the voltage ripple is 2.5 V.

The voltage modulation wave U_{au_M} and the normalized value U_{au_PWM} of the port level of the au bridge arm module are shown in Fig. 13. It can be noticed that U_{au_PWM} includes input frequency and output frequency, and the two frequencies are coupled with each other.

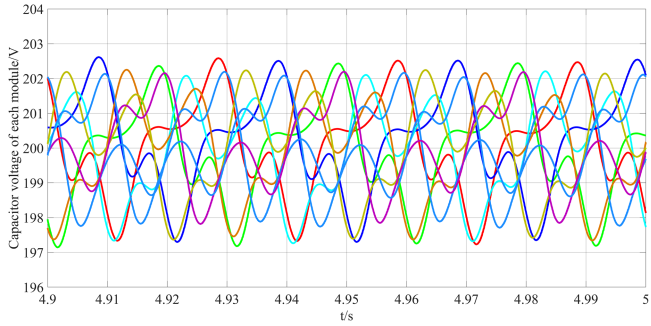

Fig. 12. Capacitor voltage of each module under DFM.

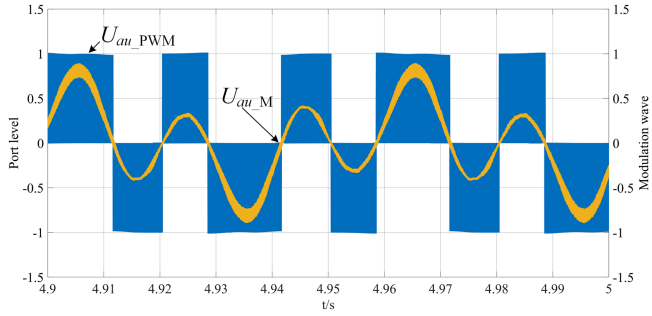

Fig. 13. Bridge arm modulation wave and port level under DFM.

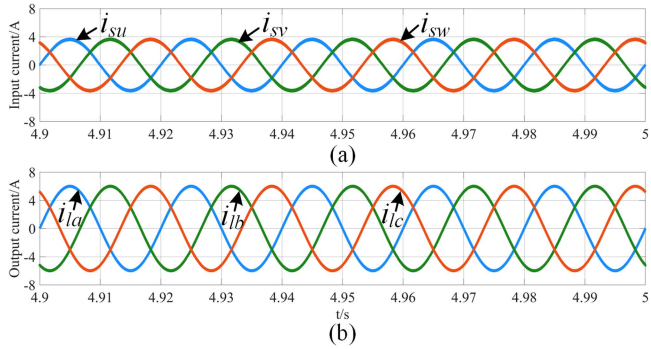

Fig. 14. Three-phase current under EFM.

B. Equal Frequencies Mode (EFM)

In the simulation model, the output frequency f_l is set to the grid voltage frequency 50 Hz, the remaining simulation parameters are the same as DFM. The three-phase currents are shown in Fig. 14.

Where the input currents are shown in Fig. 14(a), and the THD of i_{su}, i_{sv}, and i_{sw} are 1.92%, 1.92%, and 1.93%, respectively. The output currents are shown in Fig. 14(b), and the THD of i_{la}, i_{lb},and i_{lc} are 0.53%. This indicates that the proposed method will not cause harmonic pollution to the power grid under EFM.

The voltage and current are shown in Fig. 15. It can be noticed from Fig. 15(a) that the phase of the input voltage U_{su} and current i_{su} are the same, which means the system still operates under unit power factor under EFM. The output voltage and current are shown in Fig. 15(b), with the resistive system output.

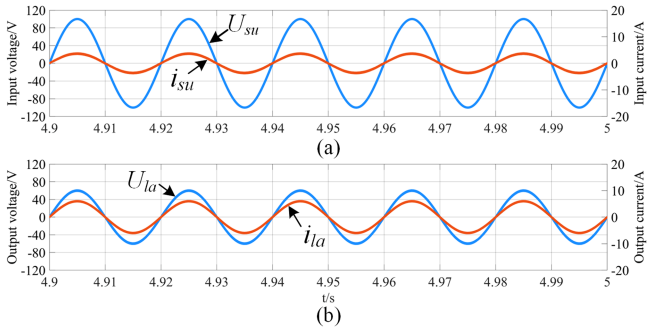

Fig. 15. Input and output voltage and current under EFM.

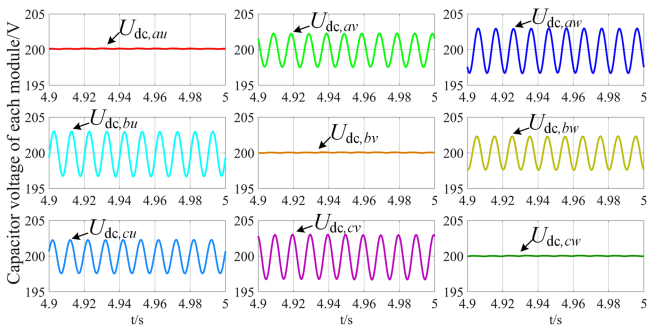

Fig. 16. Capacitor voltage of each module under EFM.

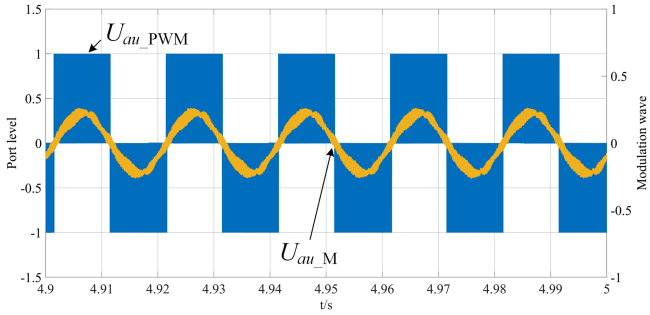

Fig. 17. Bridge arm modulation wave and port level under EFM.

The dc capacitor voltage of each module is shown in Fig. 16. It can be noticed that the dc capacitor voltage remains stable at the reference value of 200 V dc voltage. Due to the redistribution of power between bridge arms, the current amplitudes of each bridge arm are different. Therefore, the ripple of the capacitor voltage in each module also differs, showing a diagonal distribution. It can be observed that the maximum capacitor voltage ripple occurs in the bridge arms of aw, bu, and cv. The peak-to-peak value of the dc capacitor ripple of the bu bridge arm is 4.29 V.

The voltage modulation wave U_{au_M} and the normalized value U_{au_PWM} of the port level of the au bridge arm module are shown in Fig. 17. The modulated wave U_{au_M} is a sine wave under EFM. The modulation wave U_{au_M} is outputted in phase with the bridge arm port level U_{au_PWM} .

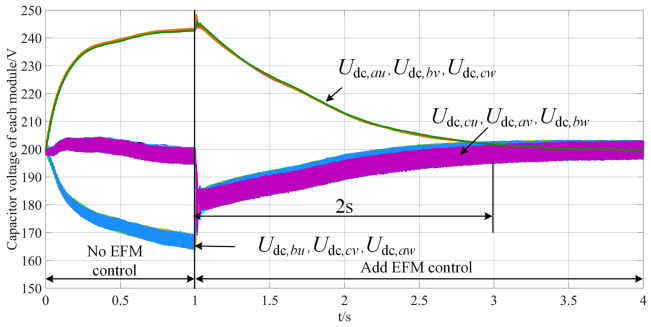

Fig. 18. Comparison of capacitor voltage under control switching.

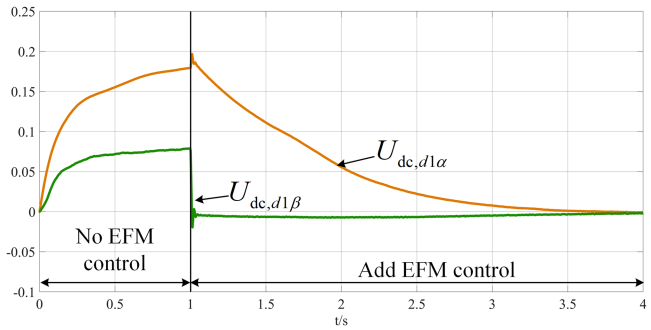

Fig. 19. Comparison of capacitor voltage difference frequency components $U_{dc,d1\alpha}$ and $U_{dc,d1\beta}$.

To verify the effectiveness of the equal frequency control strategy, comparative experiments were conducted in the simulation model. Before t=1s, there was no equal frequency control added to M^3 C control, and at t=1s, an equal frequency control strategy was added.

From Fig. 18, it can be noticed that before the EFM control is added, the capacitor voltage continuously diverges over time, with the highest capacitance–voltage reaching 250 V and the lowest capacitance–voltage reaching 164 V. The degree of voltage divergence is very severe. After the EFM control is added, adjust the capacitor–voltage value back to the capacitor voltage reference value within 2 s.

What is more, the differential frequency component of the capacitor voltage $U_{dc,d1\alpha}$ and $U_{dc,d1\beta}$ in the control system before and after control switching are shown in Fig. 19. It can be noticed that $U_{dc,d1\alpha}$ and $U_{dc,d1\alpha}$ are becoming direct flow before the EFM control is added, and increasing over time. After adding EFM control, $U_{dc,d1\alpha}$ and $U_{dc,d1\beta}$ are adjusted to 0 with the control system. The above analysis indicates that the control strategy proposed in this article can effectively balance the power of the bridge arm and achieve stable operation of the M^{3}C system at special operating points of equal frequency.

V. Experimental Results

A M^{3}C platform is performed to verify the effectiveness of the proposed method. Fig. 20 shows the photograph of the experimental prototype. Nine separate full H-bridge cells with a SiC MOSFET module (P3M12080) are connected to form the

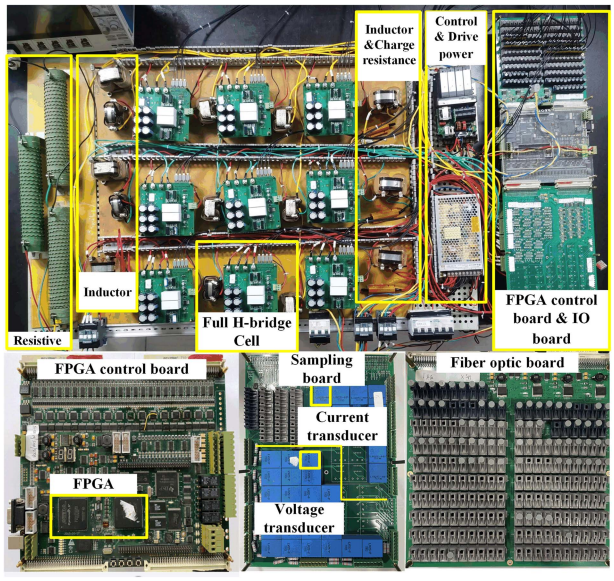

Fig. 20. Experimental setup of the M^3C.

TABLE II
CIRCUIT PARAMETERS OF THE EXPERIMENTAL SETUP

Parameters	Symbol	Value
Input phase voltage (peak value)	U_s	100 V
Output phase voltage (peak value)	U_l	60 V
DC capacitor voltage	$U_{\rm dc}$	200 V
Input frequency	f_s	50 Hz
Output frequency (DFM)	f_l	17 Hz
Output frequency (EFM)	f_l	50 Hz
Input/Output filter inductance	$\rm L_{u,v,w,a,b,c}$	5 mH
Bridge arm inductance	$\rm L_{arm}$	1 mH
Charge resistance	$\rm R_{charge}$	100 Ω/200 W
Three phase load	$\rm R_{a,b,c}$	10 Ω
H-bridge DC capacitance	C	990 μF
Switching frequency	f	8 kHz

adopted M^3C. Fifteen LEM LA25-NP current transducers and fifteen LEM LV25-P voltage transducers are used to sample the six input/output currents and voltages, nine capacitor voltages, and nine bridge arm currents, respectively. The control methods are programmed in field programmable gate array (FPGA) EP5CEFA7F31C8 and the parameters of the experimental setup are listed in Table II. The temperature distribution of the M^3 C is shown in Fig. 21.

A. Different Frequencies Mode (DFM)

The steady-state experimental results of the proposed method under DFM are shown in Fig. 22. It can be noticed that the input and output currents are sinusoidal, and the dc capacitor voltage is stable at the reference value of 200 V. The THD of i_{su}, i_{sv}, and i_{sw} are 2.8%, 2,9%, and 3.0%, meanwhile, the THD of i_{la}, i_{lb}, and i_{lc} are 2.1%, 2.0%, and 2.0%, respectively. The

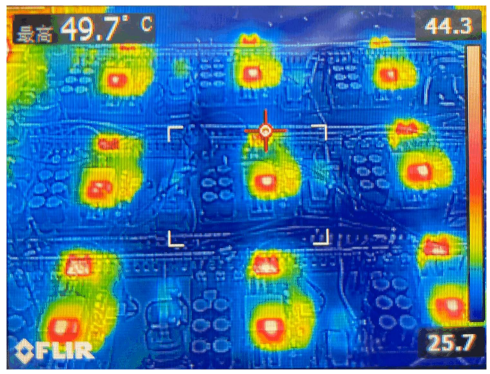

Fig. 21. Temperature distribution of M^3C.

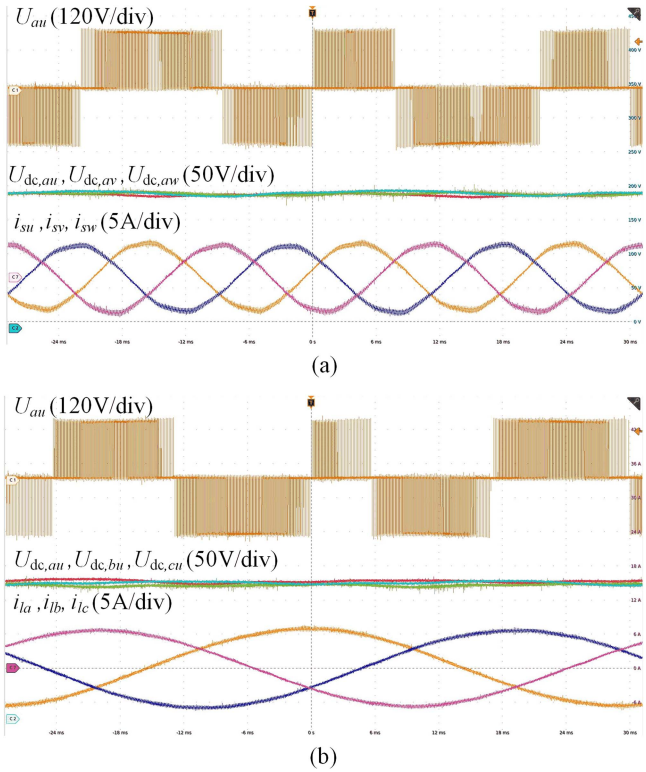

Fig. 22. Steady-state experimental results of the proposed method under DFM: (a) input side; (b) output side.

control system designed in this article has a good steady-state performance.

The experimental results of bridge arm currents under DFM are shown in Fig. 23. It can be noticed from Fig. 23(a) that the combined frequency of i_{au}, i_{bu}, and i_{cu} is the same as i_{su}. From Fig. 23(b), it can be noticed that the combined frequency of i_{au}, i_{av}, and i_{aw} is the same as i_{la}, i.e., the current distribution indicated by (5).

B. Equal Frequencies Mode (EFM)

The steady-state experimental results of the proposed method under EFM are shown in Fig. 24. It can be noticed that the input and output currents are sinusoidal, and the dc capacitor voltage

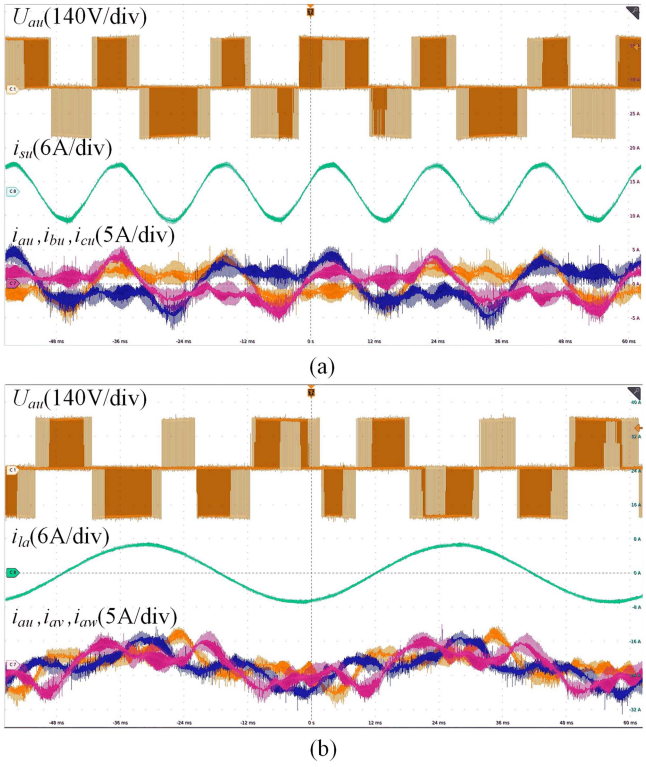

Fig. 23. Bridge arm currents under DFM: (a) input side; (b) output side.

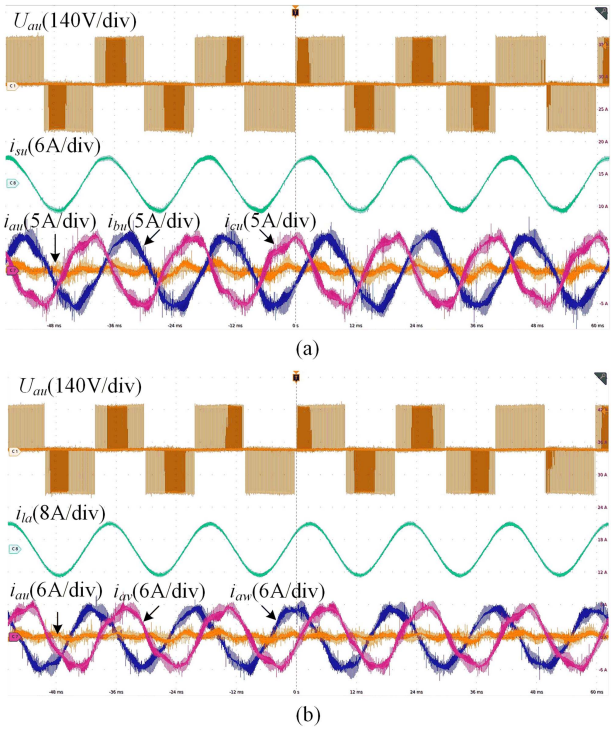

Fig. 25. Bridge arm currents under EFM: (a) input side; (b) output side.

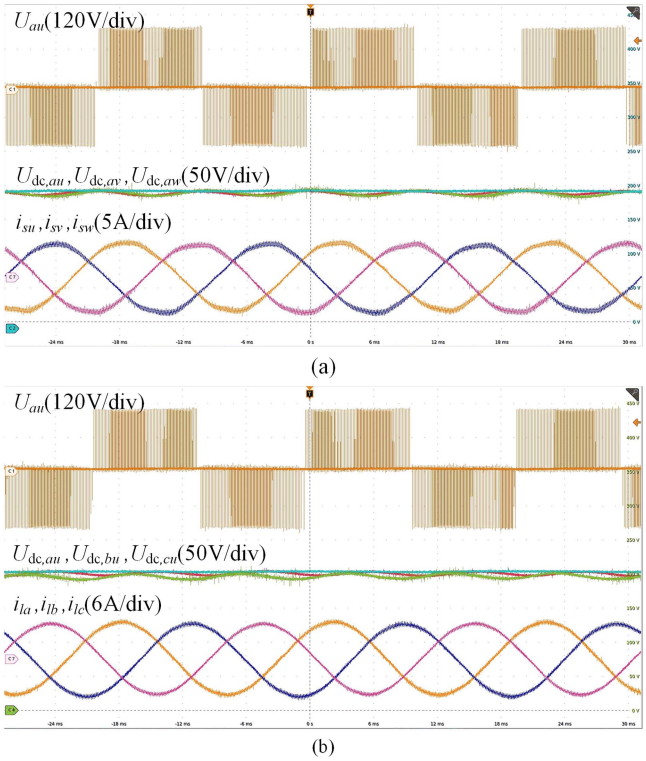

Fig. 24. Steady-state experimental results of the proposed method under EFM: (a) input side; (b) output side.

is stable at the reference value of 200 V. The THD of i_{su}, i_{sv}, and i_{sw} are 2.7%, 2,6%, and 2.9%, meanwhile, the THD of i_{la}, and i_{lb}, i_{lc} are 1.4%, 1.5%, and 1.5%, respectively.

The experimental results of bridge arm currents under DFM are shown in Fig. 25. It can be noticed that the equal frequency control strategy needs to control the circulating current for power compensation, and the circulating current component has a significant impact on the current of each bridge arm. The effective current value of the au bridge arm is only 0.7 A. The input current of the U-phase is mainly distributed in the bu and cu bridge arms, while the output current of the A-phase is mainly distributed in the av and aw bridge arms.

What's more, the experimental results of equal frequency control switching are shown in Fig. 26. Cut off the equal frequency control at time t1, and then the capacitor voltage begins to diverge. After stabilizing, the dc capacitor voltages of the au, bu, and cu bridge arms are 275 V, 154 V, and 164 V, respectively. Without equal frequency control, the maximum difference in dc capacitor voltage of the bridge arm is 121 V, indicating a significant dc voltage difference. At time t2, the equal frequency control was reintroduced and after 8 s, the dc capacitor voltage of each bridge arm was restored to a balanced state.

Moreover, to verify the dynamic performance of the control strategy, an output voltage reference value jump experiment proceeded, as shown in Fig. 27. It can be noticed from Fig. 27(a) that the output voltage and current of the system vary steadily during the jumping process, without any obvious overshoot phenomenon. The detailed waveforms under 40 and 80 V voltage are shown in Fig. 27(b) and (c), respectively. From Fig. 27(d),

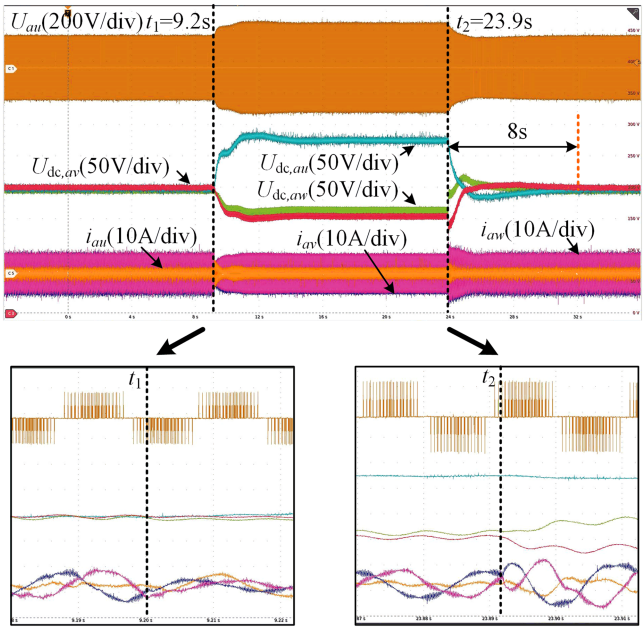

Fig. 26. Experimental results of equal frequency control switching.

it can be noticed that the input current smoothly transitions to the next state without obvious oscillation, and there is a certain fluctuation in the dc capacitor voltage. The maximum overshoot voltage is 12 V, with a fluctuation of 6%.

The experimental results show that the control method proposed in this article can quickly adjust the dc voltage to maintain stability, and effectively control the changes in input voltage and output voltage and current during the switching process, with a good dynamic response.

C. Output Frequency Changing Condition

The experiment of output frequency changing condition is also proceed in this article, as shown in Figs. 28 and 29. At time 0–t1, the output frequency f_l is 17 Hz. At time t1, the output frequency f_l jumps to 50 Hz. At time t1–t2, the system remains in an equal frequency condition. At time t2, the output frequency f_l jumps to 67 Hz.

From Fig. 28, it can be noticed that the output voltage and output current jump to 50 and 67 Hz within one cycle, and the system output voltage and current amplitude stabilize again to the given value within 2 s.

From Fig. 29, it can be noticed that during the process of the output frequency f_l jumping from 17 to 50 Hz and then to 67 Hz, the capacitor voltage stabilizes again at the reference value within 3 s and 5 s, respectively. During the process of changing the output frequency, the input current remains basically stable, indicating that the control strategy proposed in this article has the ability of variable frequency operation and good dynamic performance.

To sum up, the performance comparison of the proposed and conventional method is shown in Table III. From Table III, it can be noticed that the central controller of conventional methods is DSP and FPGA, while this article only uses FPGA as central

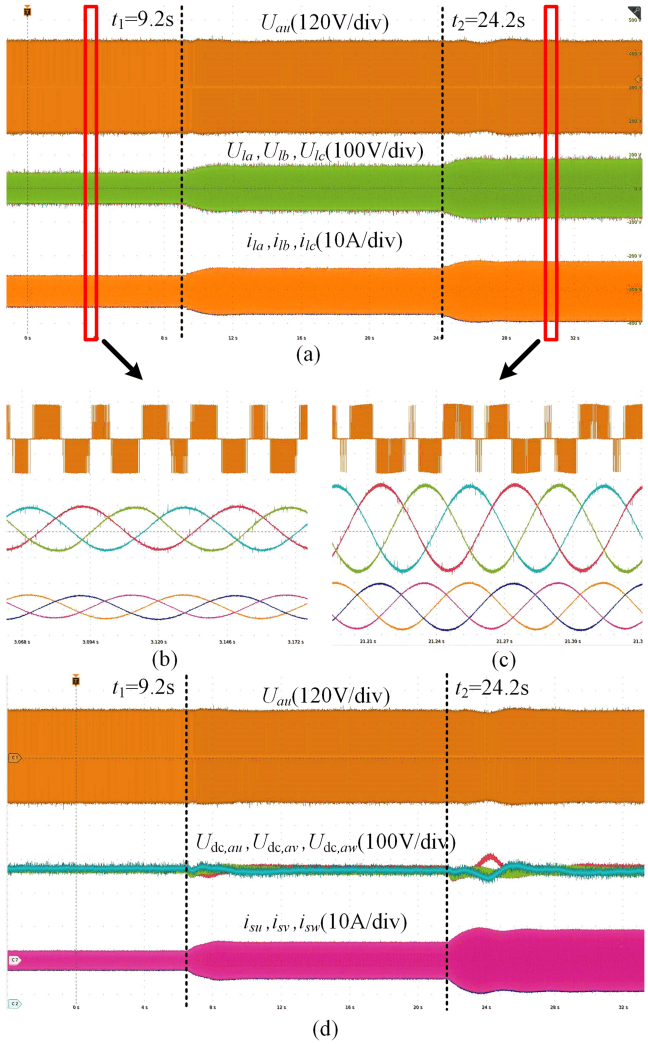

Fig. 27. Experimental results of output voltage reference value jump: (a) output voltage and current; (b) detailed waveforms under 40 V output voltage; (c) detailed waveforms under 80 V output voltage; (d) input current and bridge arm voltage.

TABLE III
PERFORMANCE COMPARISON OF PROPOSED AND CONVENTIONAL METHODS

Performance	Control methods				
	Method in [20]	Method in [22]	Method in [24]	Method in [26]	Proposed method
Central controller	DSP&FPGA	DSP&FPGA	DSP&FPGA	DSP&FPGA	FPGA
Control method	PI control	PI control	PI control	PI control & MPC	PI control
Common-mode voltage injection	No	Yes	No	Yes	No
Output side reactive power control	Required $Q_s = -Q_l$	Not Required	Not Required	Not Required	Not Required
DC capacitor voltage stability	/	/	/	/	✓
Module Capacitance	1.7 mF	4.7 mF	0.88 mF	0.88 mF	0.99 mF

controller. What' more, the MPC method in [26] requires both PI control and model predictive control. Meanwhile, the proposed method only requires PI controller. Furthermore, compared to methods in [22] and [26], the proposed method does not require injection of common mode voltage, and compared to method in [20], the proposed method does not require additional output side reactive power control.

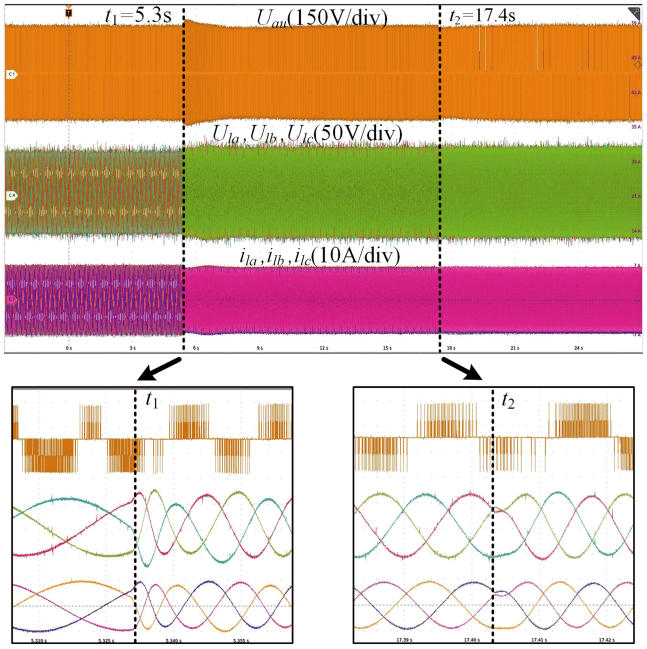

Fig. 28. Output voltage and current under output frequency change.

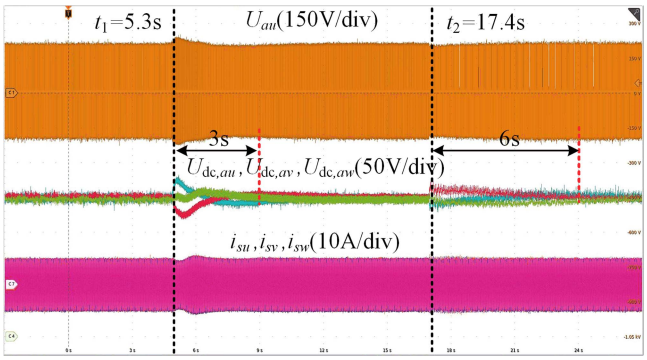

Fig. 29. Input current and bridge arm voltage under output frequency change.

VI. Conclusion

In order to address the dc capacitor voltage unbalancing caused by EFM, this article proposed a low-frequency circulating current injection method in eight-component control for a modular multilevel matrix converter. The low-frequency circulation current consists of frequency components present in the system. Through experimental verification, this method can achieve dc capacitor voltage balance and stable operation both under different and equal frequency conditions. What's more, the dynamic performance of the proposed control method is also good. Under equal frequency conditions, after cutting off the equal frequency control and putting it back into operation, the capacitor voltage only needs 8 s to recover the reference value. Under the conditions of output voltage voltage or frequency change, the output currents remain stable and the capacitor voltage returns to stability within 6 s.

References

[1] M. A. Perez, S. Bernet, J. Rodriguez, S. Kouro, and R. Lizana, "Circuit topologies, modeling, control schemes, and applications of modular multilevel converters," *IEEE Trans. Power Electron.*, vol. 30, no. 1, pp. 4–17, Jan. 2015.

[2] M. Winkelnkemper, A. Korn, and P. Steimer, "A modular direct converter for transformerless rail interties," in *Proc. IEEE Int. Symp. Ind. Electron.*, 2010, pp. 562–567.

[3] R. Marquardt, "Modular multilevel converter: An universal concept for HVDC-networks and extended DC-bus-applications," in *Proc. Int. Power Electron. Conf.-ECCE ASIA*, 2010, pp. 502–507.

[4] J. Liu, S. Yue, W. Yao, W. Li, and Z. Lu, "DC voltage ripple optimization of a single-stage solid-state transformer based on the modular multilevel matrix converter," *IEEE Trans. Power Electron.*, vol. 35, no. 12, pp. 12801–12815, Dec. 2020.

[5] S. Jayasinghe and D. Vilathgamuwa, "A modular matrix converter for transformer-less PMSG wind generation systems," in *Proc. IEEE Ninth Int. Conf. Power Electron. Drive Syst.*, 2011, pp. 474–479.

[6] M. Díaz, R. Cardenas, B. Mauricio Espinoza, A. Mora, and F. Rojas, "A novel LVRT control strategy for modular multilevel matrix converter based high-power wind energy conversion systems," in *Proc. Tenth Int. Conf. Ecological Veh. Renewable Energies*, 2015, pp. 1–11.

[7] H. Akagi, "Classification, terminology, and application of the modular multilevel cascade converter (MMCC)," *IEEE Trans. Power Electron.*, vol. 26, no. 11, pp. 3119–3130, Nov. 2011.

[8] A. Christe, A. Faulstich, M. Vasiladiotis, and P. Steinmann, "World's first fully rated direct AC/AC MMC for variable-speed pumped-storage hydropower plants," *IEEE Trans. Ind. Electron.*, vol. 70, no. 7, pp. 6898–6907, Jul. 2023.

[9] J. E. Huber and J. W. Kolar, "Applicability of solid-state transformers in today's and future distribution grids," *IEEE Trans. Smart Grid*, vol. 10, no. 1, pp. 317–326, Jan. 2019.

[10] F. Kammerer, J. Kolb, and M. Braun, "A novel cascaded vector control scheme for the modular multilevel matrix converter," in *Proc. 2011-37th Annu. Conf. IEEE Ind. Electron. Soc.*, 2011, pp. 1097–1102.

[11] F. Kammerer, J. Kolb, and M. Braun, "Fully decoupled current control and energy balancing of the modular multilevel matrix converter," in *Proc. 15th Int. Power Electron. Motion Control Conf.*, 2012, pp. LS2a.3-1–LS2a.3-8.

[12] Y. Hayashi, T. Takeshita, M. Muneshima, and Y. Tadano, "Independent control of input current and output voltage for modular matrix converter," in *Proc. 39th Annu. Conf. IEEE Ind. Electron. Soc.*, 2013, pp. 888–893.

[13] T. Nakamori, M. A. Sayed, Y. Hayashi, T. Takeshita, S. Hamada, and K. Hirao, "Independent control of input current, output voltage, and capacitor voltage balancing for a modular matrix converter," *IEEE Trans. Ind. Appl.*, vol. 51, no. 6, pp. 4623–4633, Nov./Dec. 2015.

[14] Y. Meng, S. Li, Y. Zou, K. Li, and X. F. Wang, "Stability analysis and control optimization based on particle swarm algorithm of modular multilevel matrix converter in fractional frequency transmission system," *IET Gener. Transmiss. Distrib.*, vol. 14, no. 4, pp. 2641–2655, 2020.

[15] F. Kammerer, M. Gommeringer, J. Kolb, and M. Braun, "Energy balancing of the modular multilevel matrix converter based on a new transformed arm power analysis," in *Proc. 16th Eur. Conf. Power Electron. Appl.*, 2014, pp. 1–10.

[16] D. Braeckle, F. Kammerer, M. Schnarrenberger, M. Hiller, and M. Braun, "A modular multilevel matrix converter for high speed drive applications," in *Proc. PCIM Europe 2016; Int. Exhib. Conf. Power Electron., Intell. Motion, Renewable Energy Energy Manage.*, 2016, pp. 1–8.

[17] Y. Miura, K. Inubushi, T. Yoshida, T. Fujikawa, and T. Ise, "Operation of modular matrix converter under close input and output frequency by using voltage space vector modulation," in *Proc. 41st Annu. Conf. IEEE Ind. Electron. Soc.*, 2015, pp. 005136–005141.

[18] Y. Miura, T. Mizutani, M. Ito, and T. Ise, "A novel space vector control with capacitor voltage balancing for a multilevel modular matrix converter," in *Proc. IEEE ECCE Asia Downunder*, 2013, pp. 442–448.

[19] Y. Miura, K. Inubushi, M. Ito, and T. Ise, "Multilevel modular matrix converter for high voltage applications: Control, design and experimental characteristics," in *Proc. 40th Annu. Conf. IEEE Ind. Electron. Soc.*, 2014, pp. 4690–4696.

[20] W. Kawamura, Y. Chiba, M. Hagiwara, and H. Akagi, "Experimental verification of an electrical drive fed by a modular multilevel TSBC converter when the motor frequency gets closer or equal to the supply frequency," *IEEE Trans. Ind. Appl.*, vol. 53, no. 3, pp. 2297–2306, May/Jun. 2017.

[21] W. Kawamura, M. Hagiwara, and H. Akagi, "Control and experiment of a modular multilevel cascade converter based on triple-star bridge cells," *IEEE Trans. Ind. Appl.*, vol. 50, no. 5, pp. 3536–3548, Sep./Oct. 2014.
[22] M. Diaz et al., "Vector control of a modular multilevel matrix converter operating over the full output-frequency range," *IEEE Trans. Ind. Electron.*, vol. 66, no. 7, pp. 5102–5114, Jun. 2019.
[23] S. Yue, Y. Ji, Q. Wang, and W. Yao, "Closed-loop decoupled control and implementation of the modular multilevel matrix converter in similar/equal frequency operation," in *IEEE 9th Int. Power Electron. Motion Control Conf.*, 2020, pp. 3385–3390.
[24] B. Fan, K. Wang, P. Wheeler, C. Gu, and Y. Li, "A branch current reallocation based energy balancing strategy for the modular multilevel matrix converter operating around equal frequency," *IEEE Trans. Power Electron.*, vol. 33, no. 2, pp. 1105–1117, Feb. 2018.
[25] S. Liu, B. Zhao, Y. Chen, G. Wang, and X. Wang, "Optimal arm current reallocation of modular multilevel matrix converter dedicated for power grid interconnection," *IEEE Trans. Power Del.*, vol. 37, no. 5, pp. 3477–3490, Oct. 2022.
[26] B. Fan, K. Wang, P. Wheeler, C. Gu, and Y. Li, "An optimal full frequency control strategy for the modular multilevel matrix converter based on predictive control," *IEEE Trans. Power Electron.*, vol. 33, no. 8, pp. 6608–6621, Aug. 2018.
[27] M. Urrutia, R. Cárdenas, J. C. Clare, M. Díaz, and A. Watson, "Continuous set model predictive control for energy management of modular multilevel matrix converters," *IEEE Trans. Power Electron.*, vol. 37, no. 5, pp. 5731–5748, May 2022.
[28] R. Cuzmar, A. Montenegro, A. Mora, J. Pereda, and R. P. Aguilera, "Constrained MPC for intercluster energy control of modular multilevel matrix converters," *IEEE Trans. Ind. Electron.*, vol. 71, no. 7, pp. 7766–7776, Jul. 2024.

Siyang Liu (Graduate Student Member, IEEE) received the B.S. degree in electrical engineering and automation from the School of Electrical and Electronic Engineering, Southwest Jiaotong University, Chengdu, China, in 2017. He is currently working toward the Ph.D. degree in electrical engineering at Southwest Jiaotong University. His research interests include the control and modulation of Modular Multilevel Matrix Converter and Cascaded H-Bridge Rectifier.

Haotian Zhu received the B.S. degree in electrical engineering and automation from the School of Electrical and Electronic Engineering, Southwest Jiaotong University, Chengdu, China, in 2021. He is currently working toward the M.S. degree in electrical engineering with Southwest Jiaotong University, Chengdu, China. His research interests include the control and modulation of Modular Multilevel Matrix Converter, and topology and control of power electronic traction transformer.

Xiangyu Zhao received the B.S. degree in electrical engineering and automation from the School of Electrical and Electronic Engineering, Xi'an University of technology, Xi'an, China, in 2023. He is currently working toward the master's degree in electrical engineering at Southwest Jiaotong University. His research interests include the control and modulation of Modular Multilevel Matrix Converter and Cascaded H-Bridge Rectifier.

Jiangpeng Yang (Student Member, IEEE) received the B.S. degree in electrical engineering and automation from Shenyang University of Technology, Shenyang, China, in 2019. He is currently working toward the Ph.D. degree in electrical engineering with Southwest Jiaotong University, Chengdu, China. His research interests include modulation and control techniques of multiport converter and the control techniques of unified power quality conditioner.

Jianglin Nie received the B.S. and M.S degrees in electrical engineering from the Southwest Jiaotong University, Chengdu, China, in 2019 and 2022, respectively. He is currently working toward the Ph.D. degree in electrical engineering from the Southwest Jiaotong University. His main research interests include battery balancing, power electronics converters.

Zeliang Shu (Senior Member, IEEE) received the B.S. and Ph.D. degrees from the School of Electrical Engineering, Southwest Jiaotong University, Chengdu, China, in 2002 and 2007, respectively. From 2008 to 2009, he was a lecturer with SWJTU, where he is currently a Professor Ph.D. supervisor with the School of Electrical Engineering. He was promoted to an Associate Professor and a Professor in 2009 and 2013, respectively. His research interests include active power filters, multilevel converters, pulsewidth modulation rectifier, and digital signal processing with applications to power electronic converters.